

Instability waves and transition in adverse-pressure-gradient boundary layersRikhi Bose,^{1,2,*} Tamer A. Zaki,² and Paul A. Durbin¹¹*Aerospace Engineering, Iowa State University, Ames, Iowa 50011, USA*²*Mechanical Engineering, Johns Hopkins University, Baltimore, Maryland 21218, USA*

(Received 12 December 2017; published 29 May 2018)

Transition to turbulence in incompressible adverse-pressure-gradient (APG) boundary layers is investigated by direct numerical simulations. Purely two-dimensional instability waves develop on the inflectional base velocity profile. When the boundary layer is perturbed by isotropic turbulence from the free stream, streamwise elongated streaks form and may interact with the instability waves. Subsequent mechanisms that trigger transition depend on the intensity of the free-stream disturbances. All evidence from the present simulations suggest that the growth rate of instability waves is sufficiently high to couple with the streaks. Under very low levels of free-stream turbulence ($\sim 0.1\%$), transition onset is highly sensitive to the inlet disturbance spectrum and is accelerated if the spectrum contains frequency-wave-number combinations that are commensurate with the instability waves. Transition onset and completion in this regime is characterized by formation and breakdown of Λ vortices, but they are more sporadic than in natural transition. Beneath free-stream turbulence with higher intensity (1–2%), bypass transition mechanisms are dominant, but instability waves are still the most dominant disturbances in wall-normal and spanwise perturbation spectra. Most of the breakdowns were by disturbances with critical layers close to the wall, corresponding to inner modes. On the other hand, the propensity of an outer mode to occur increases with the free-stream turbulence level. Higher intensity free-stream disturbances induce strong streaks that favorably distort the boundary layer and suppress the growth of instability waves. But the upward displacement of high amplitude streaks brings them to the outer edge of the boundary layer and exposes them to ambient turbulence. Consequently, high-amplitude streaks exhibit an outer-mode secondary instability.

DOI: [10.1103/PhysRevFluids.3.053904](https://doi.org/10.1103/PhysRevFluids.3.053904)**I. INTRODUCTION**

Traditionally, the term “bypass” has been used to classify transition processes in which Tollmien-Schlichting (TS) waves do not play a prominent role. In recent literature, bypass transition has been synonymous with the phenomenon of breakdown to turbulence in boundary layers forced by modest to high free-stream perturbations. In this case, shear acts as a low-pass filter and admits only the low-frequency disturbances into the boundary layer [1,2]. They spawn streamwise streaky distortions in the u -perturbation component. These streaks grow rapidly through shear amplification [3,4]. This nonmodal amplification of streaks means that bypass transition may be under way even before the critical Reynolds number for the TS wave is reached [5,6]. Therefore, it is understood that instability waves play no role in bypass transition.

In adverse pressure gradient (APG), the base-flow profile becomes inflectional and inviscidly unstable. Depending upon flow regime, the instability wave and Klebanoff streaks may have commensurate amplitudes. For example, nonmodal growth is weak under low-intensity free-stream

*rikhi004@gmail.com

turbulence (FST), so that the instability wave amplification ought to be relevant. Therefore, up to moderate levels of free-stream excitation, an interactional *mixed mode* of transition is expected [7–9]. Bose and Durbin [10] demonstrated that such regime can, indeed, be created, even in zero pressure gradient (ZPG). In those simulations, both a TS wave and FST were injected at the inflow, and transition occurred through their interaction. The present work examines this regime in the natural setting of an APG boundary layer, without imposing a TS wave at the inflow.

Experimental studies by Walker and Gostelow [11] and Gostelow *et al.* [12] demonstrate the complexity of transition phenomena in APG flat-plate boundary layers. Unlike bypass transition in ZPG, their experiments identified spontaneously appearing discrete instability waves beneath FST. Walker and Gostelow [11] attributed transition under low-intensity FST to subharmonic secondary instability of the naturally appearing instability waves. In another experimental effort, Hughes and Walker [13] detected instability waves in their data on transitional flow over a compressor blade, when turbulence intensity in the free stream was as high as 8%. They removed high-amplitude low-frequency disturbance components by a filtering technique, and identified instability wave packets in the residual. Hence, they speculated that the instability waves triggered breakdown to turbulent spots in regions of flow deceleration.

Similar observations have been made in computational studies. Zaki *et al.* [14] used DNS to study bypass transition in flow over a compressor blade. Instability waves could be identified in their visualizations of the disturbance flow field near the blade surface.

There is evidence of instability wave packets in the APG region after the blunt leading edge of a flat plate: Nagarajan *et al.* [15] observed instability wave packets to trigger turbulent spots in their DNS of this configuration. Strong competitive growth of exponential instability also was obtained by Corbett and Bottaro [16] in their linear optimal disturbance studies of Falkner-Skan boundary layers. They demonstrated that in APG, the optimal streamwise vortices undergo transient growth and may attain similar amplitudes as exponential instabilities, at supercritical Reynolds numbers.

All these results indicate that both natural and bypass transitions in APG boundary layers can involve instability waves. In the present study, direct simulations of an APG boundary layer are performed in regimes where both streaks and instability waves coexist and can interact.

Late stages of boundary-layer transition in ZPG were studied extensively in the literature, both experimentally and computationally. Secondary instability is activated beyond a critical amplitude of the primary instabilities. In orderly transition, secondary instability leads to formation of Λ -shaped vortices that break down into turbulent spots [17,18]. For streaks, an inviscid secondary instability analysis was developed by Andersson *et al.* [19] and others [5]. They showed that the lifted, high-amplitude, low-speed streaks are susceptible to spanwise asymmetric, sinuous instability in ZPG boundary layers. Amplification of spanwise symmetric varicose modes was predicted, only at very high streak amplitudes. Later, using Floquet stability theory, Vaughan and Zaki [20] showed that the critical layer of the most amplifying sinuous disturbances was near the edge of the boundary layer ($\sim 0.7\delta_{99}$). They also predicted another secondary instability with a critical layer closer to the wall ($\sim 0.4\delta_{99}$). Therefore, they named these as *outer* and *inner* modes, respectively. In a following DNS at FST intensity ($Tu = 3\%$), Hack and Zaki [21] verified that the turbulent spot precursors in APG are inner modes. The possible explanation for a shift in critical layer from ZPG to APG was the absence or presence of an inflection point in the base profile.

In simulations of mixed-mode transition in ZPG, Bose and Durbin [10] observed a regime, between orderly transition via Λ vortices and bypass transition via outer streak instability, in which both streaky disturbances and TS waves contributed significantly to amplifying perturbations. Breakdown via helical secondary structures was observed. The helical secondary instability is an inner mode. In that study, the base profile was not inflectional; instability waves were created at the inflow. Since APG promotes discrete exponential instabilities, one can predict that helical waves will arise naturally in decelerated flows.

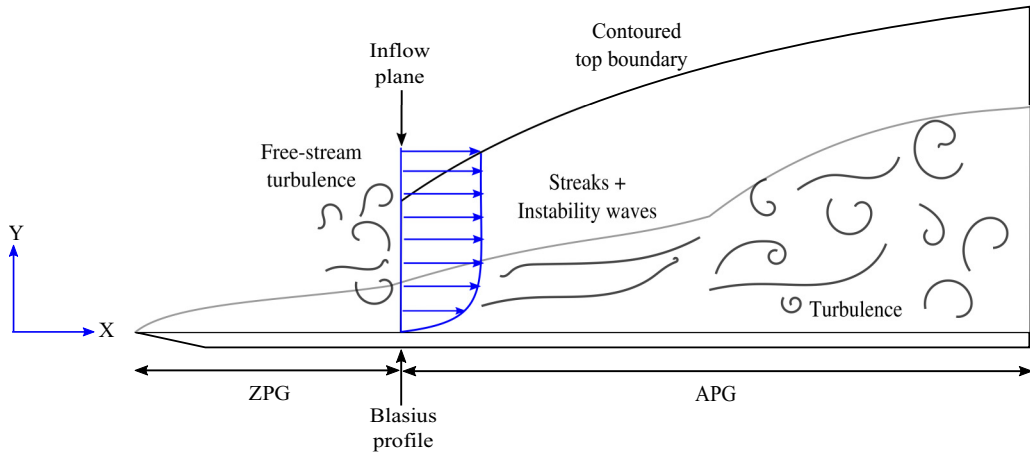


FIG. 1. Schematic of the setup simulated numerically.

A. Contribution

In the present work, direct numerical simulations of transition in adverse-pressure-gradient boundary layers are performed. In these simulations, Reynolds number and the level of APG are sufficiently high so that instability waves amplify spontaneously without explicitly injecting them at the inflow as in previous work in ZPG. The effects of free-stream turbulence spectrum and its amplitude on the transition mechanism are examined. The simulations are aimed to assess the propensity of the external forcing, at low turbulence intensities, to spawn instability waves inside the boundary layer, in a process similar to orderly transition. At moderate levels of free-stream forcing, the helical structures are sought in the mixed-mode transitional regime. At higher turbulence intensities, the simulations examine the interplay between instability waves and Klebanoff streaks. The numerical experiments were performed to demonstrate the following:

(1) Instability and transition to turbulence at very low turbulence intensities are highly sensitive to the scales of the incoming turbulence.

(2) An intermediate regime exists between natural transition beneath very-low-intensity broadband free-stream turbulence and bypass transition beneath high turbulence intensities. This regime may appear naturally without directly prescribing, or forcing, an instability wave upstream as part of the inlet spectra.

(3) The instability waves participate in transition at supercritical Reynolds numbers in APG even at relatively high turbulence intensities. When Klebanoff streak and instability wave amplitudes are of same level, instabilities of helical nature trigger transition.

(4) It is generally accepted that “inner” secondary instabilities trigger breakdown in an APG bypass transitional boundary layer. In current simulations, with increase in Klebanoff streak amplitude at higher levels of free-stream forcing, propensity of outer sinuous mode breakdown is increased. The increased proclivity is a consequence of damping of instability waves and susceptibility of high-amplitude streaks to secondary disturbance growth.

II. DIRECT NUMERICAL SIMULATIONS

The numerical technique to perform the simulations has been developed in studies of transitional and turbulent flows for more than a decade [22,23]. The simulation code solves the incompressible Navier-Stokes and continuity equations by a finite-volume formulation, on a staggered, curvilinear grid. The upper boundary is contoured to impose APG on the bottom, flat wall. The domain setup is characterized in Fig. 1.

TABLE I. Summary of simulations.

Case designation	Domain size ($l_x \times l_y \times l_z$)	Grid size ($n_x \times n_y \times n_z$)	Tu (%)	Lowest nonzero inlet frequency (ω)
1a	$320\delta_0 \times 40\delta_0 \times 20\delta_0$	$1024 \times 192 \times 160$	0.1	0.636
1b	$480\delta_0 \times 40\delta_0 \times 35\delta_0$	$1536 \times 192 \times 280$	0.1	0.357
2	$320\delta_0 \times 40\delta_0 \times 20\delta_0$	$1024 \times 192 \times 160$	1	0.636
3	$320\delta_0 \times 40\delta_0 \times 20\delta_0$	$1024 \times 192 \times 160$	2	0.636

The velocity components are solved at the faces of a computational cell and pressure at its center. A fractional step procedure is adopted. The nonlinear advection terms are advanced in time with a second-order, Adams-Bashforth scheme. Advection terms are computed by a blend of seven-tenths central differences and three-tenths QUICK, to avoid numerical oscillations. The diffusion terms are split into explicit and implicit parts. Cross derivatives on the curvilinear grid are treated explicitly and are time-advanced with second-order Adams-Bashforth. The implicit terms are advanced with Crank-Nicolson. The pressure Poisson equation is solved using a Fourier transform in the spanwise periodic direction and multigrid in the x - y plane.

The current simulations examine the effect of APG on bypass transition. To facilitate comparison with prior ZPG simulations [10], a Blasius profile at Reynolds number $Re_b = \sqrt{U_0 x_0 / \nu} = 398$ (based on momentum thickness is $Re_\theta \sim 265$) is specified at the inlet plane; thus the inlet conditions can be specified as in previous studies. Here, x_0 is the streamwise distance of the inflow plane from the leading edge. All lengths in the simulations are nondimensionalized by the 99% thickness of the Blasius boundary layer at the inlet plane, hereafter denoted as δ_0 . The velocity scale is the free-stream speed U_0 , also taken at the inflow plane. Consequently, the characteristic time scale is $\frac{\delta_0}{U_0}$. All variables mentioned in the text are nondimensionalized by these scales unless otherwise mentioned. From here onward, streamwise distance downstream of the inlet plane, nondimensionalized by δ_0 , is denoted as x .

The size of the computational domain in each direction is given in Table I for all the simulations. Detailed grid and domain independence studies are summarized in Bose [24]. The number of grid points used in each direction is also listed in Table I. The grid resolution is unchanged among all simulations. The grid resolution was found to be sufficient to resolve up to the completion of transition, but is insufficient in the fully turbulent regime.

A. Base flow and exponential instability wave

APG is induced by diverging the upper boundary of the computational domain and applying impermeability and free-slip conditions at that boundary (Fig. 1). The pressure gradient follows a power-law distribution downstream of the inlet plane, $P_\infty(x) = Kx^{2m}$. Here, m is related to Hartree parameter, $m = \beta_H / (2 - \beta_H)$. Throughout this work, $\beta_H = -0.14$, which is equal to the value used in earlier studies [21,23].

In order to characterize the pressure gradient in the simulation domain, first the laminar base flow was computed. The inflow condition was the ZPG, Blasius solution. The base flow relaxes toward a Falkner-Skan profile at the target acceleration parameter. In Fig. 2(a), the scaled streamwise velocity profile is plotted at different streamwise locations. After an initial adjustment length ($x \sim 70$), the velocity profiles are in very good agreement with the Falkner-Skan similarity solution. The pressure gradient parameter $\lambda_\theta = \frac{\theta^2}{\nu} \frac{dU_\infty}{dx}$ is a good measure of the imposed streamwise pressure gradient. In this expression, $U_\infty(x)$ is the local free-stream speed. In Fig. 2(b), λ_θ is plotted against streamwise distance x . After an initial adjustment, λ_θ remains constant. The imposed pressure gradient level matches well with the target $\beta_H = -0.14$.

At $\beta_H = -0.14$, the velocity profile is inflectional, which significantly lowers the critical Reynolds number and enhances instability [25]. An exponentially unstable wave with very small magnitude

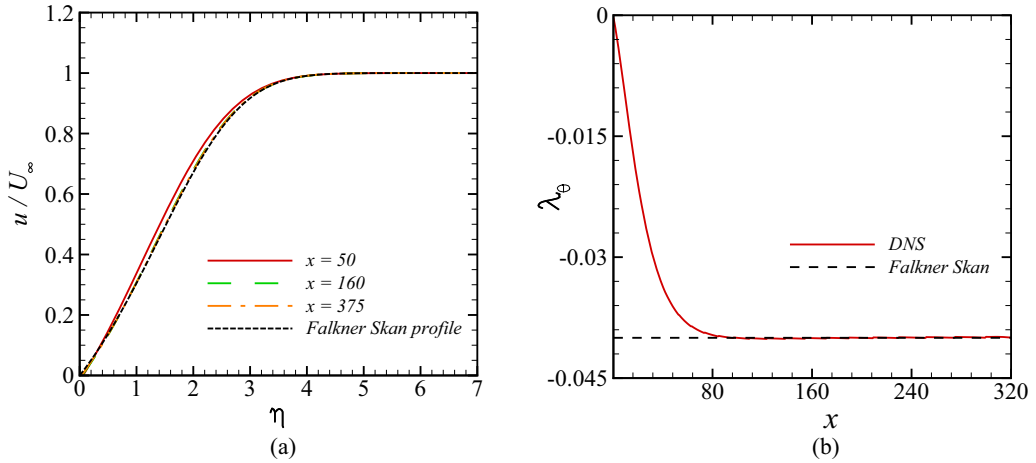


FIG. 2. (a) $u/U_\infty(x)$ plotted against the similarity variable η at select streamwise stations. (b) Pressure gradient parameter λ_θ plotted against x .

is excited spontaneously, inside the computational domain. The unstable wave grows sufficiently fast to become nonlinear. The instantaneous streamwise and wall-normal perturbation velocities, u' and v' , at a wall normal height $y = \delta_0/2$ are plotted in Fig. 3(a). Near $x = 400$, the magnitude of u' attains a value as high as 1% of the inlet free-stream velocity.

Frequency spectra of u' and v' components were computed at $x = 210$, where the amplitude of the instability wave is small. The disturbances are linear at this location. The peak amplitude was obtained at $\omega = 0.11$. Another broad peak was obtained close to $\omega = 0.22$; higher harmonics are also excited.

In Fig. 3(b), contours of amplification rate (k_i) for the spatially most unstable mode from the discrete spectrum of the OS equation are plotted in the $(Re_{\delta_*}, \omega_{\delta_*})$ plane for the Falkner-Skan boundary

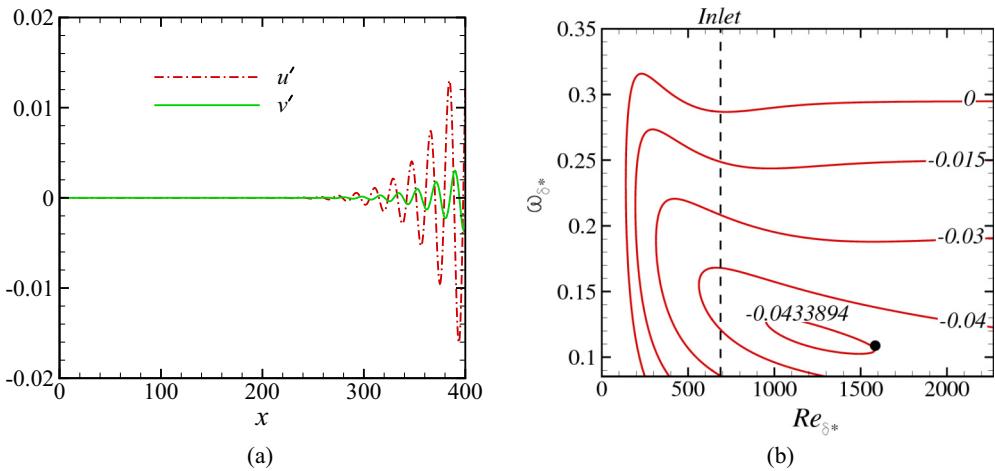


FIG. 3. (a) Instantaneous u' and v' plotted against x at $y = \delta_0/2$. (b) Contours of the growth rate (k_i) of the most unstable mode as a function of Reynolds number Re_{δ_*} and frequency ω_{δ_*} for the Falkner-Skan boundary layer with $\beta_H = -0.14$. The reference scales are displacement thickness δ_* and local free-stream speed U_∞ . The vertical dashed line indicates the Reynolds number at the inlet plane. The unstable mode from DNS at $x = 210$ is marked by the black dot.

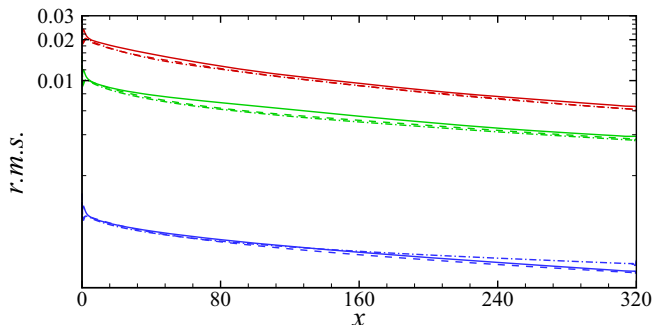


FIG. 4. Free-stream decay of rms value of u' (solid), v' (dashed), and w' (dash-dotted) for cases 1a (blue), 2 (green), and 3 (red).

layer with $\beta_H = -0.14$. The reference scales are the displacement thickness δ_* and free-stream speed U_∞ . At the Reynolds number Re_{δ_*} at $x = 210$, the value of ω_{δ_*} which corresponds to $\omega = 0.11$ (observed in DNS) is marked by the filled circle. The frequency from the DNS is very close to that of the locally most unstable instability wave.

The theoretical wavelength calculated from the real part of the complex wave number obtained from the linear stability theory [the imaginary part is plotted in Fig. 3(b)] is $17.91\delta_0$; in the DNS $18.25\delta_0$ was observed.

B. Inlet FST

Inlet free-stream turbulence was synthesized as a superposition of eigenmodes of the linear perturbation equations [26,27]. The number of eigenmodes was 32 in each of temporal frequency, wall-normal wave number, and spanwise wave number. The spectral amplitudes satisfy isotropy and continuity. The inlet condition is synthesized to reproduce a Von-Karman energy spectrum with the peak at wave number $k_p \sim 1$ (nondimensionalized by the streamwise integral scale, L_{11}). This method of inlet FST generation is regularly used for studies of bypass transition, as it reduces the computational cost by circumventing the high grid resolution, and numerical inaccuracy, that occur near a leading edge.

Three levels of FST intensity, $\text{Tu} = \sqrt{(u_{\text{rms}}^2 + v_{\text{rms}}^2 + w_{\text{rms}}^2)/3} = \{0.1, 1.0, 2.0\}\%$, were applied at the inflow plane. The simulation parameters are listed in Table I. The downstream evolution of rms values of u' , v' , and w' in the free stream are shown in Fig. 4 for cases 1a, 2, and 3. Turbulence remains fairly isotropic in the free stream, throughout the domain, for all three cases.

The spectral content in cases 1a, 2, and 3 is identical. For case 1b, the lowest frequency is reduced relative to case 1a, but the turbulence intensity is unchanged. The inlet energy spectra for cases 1a and 1b are compared in Fig. 5, where they are plotted against the temporal frequency ω in Fig. 5(a) and spanwise wave number k_z in Fig. 5(b). The amplitudes of the zero-frequency modes are set to zero to avoid base-flow distortion. The number of inlet frequency modes is identical for both these cases. Inlet disturbances for case 1a have more high-frequency components. Low-frequency disturbances are more energetic for case 1b. As purely two-dimensional (2D) instability waves ($k_z = 0$) were spontaneously instigated while computing the base flow, they were excluded from the inlet disturbance spectra to avoid augmentation of the amplitude of the instability waves.

The integral of the energy spectral density $E(\kappa)$, where κ is the magnitude of the three-dimensional wave-number vector, over a sphere in wave-number space gives the kinetic energy:

$$\int_0^\infty E(\kappa) d\kappa = \frac{1}{2} \int_0^\infty 4\pi\kappa^2 (\hat{u}\hat{u}^* + \hat{v}\hat{v}^* + \hat{w}\hat{w}^*) d\kappa.$$

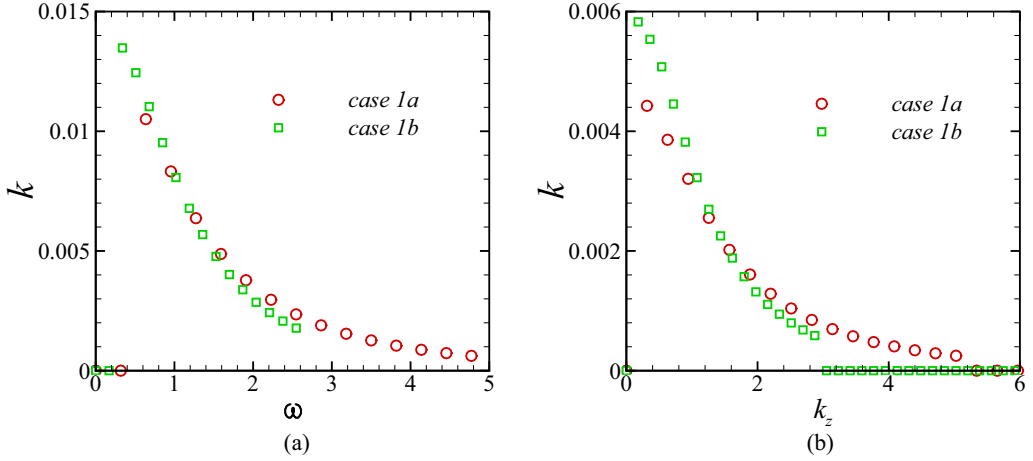


FIG. 5. (a) Disturbance kinetic energy at inlet as a function of (a) frequency (ω) and (b) spanwise wave number (k_z) for the cases 1a and 1b (see Table I).

The energy E as a function of κ is plotted for cases 1a and 1b in Fig. 6. Each symbol in this figure represents an individual disturbance mode. It is evident that the inlet disturbances for case 1b contain more large-scale modes even though Tu is the same for these two cases. The inlet spectral content has profound effect on the transition process, as is discussed in the next section.

III. FREE-STREAM EXCITATION

Four direct numerical simulations were performed with the conditions and designations listed in Table I. In Fig. 7(a), instantaneous skin-friction coefficient C_f is plotted against Re_x for all cases, at a single spanwise location. The relationship between Re_x and x is $Re_x = \frac{(1 + \frac{x}{x_1})^m (x + x_0)}{\nu} = 2556.9(x + 81.34)(x + 58.19)^{-0.0654}$. Here, x_0 is the distance of the inflow plane from the leading

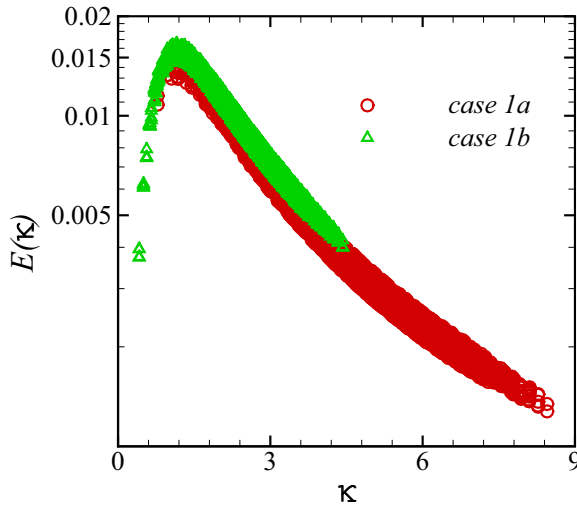


FIG. 6. Energy spectral density, $E(\kappa)$, of inlet perturbations plotted against κ for the cases 1a and 1b. Each symbol represents an inlet disturbance mode. Only half of the total number of modes is plotted for clarity.

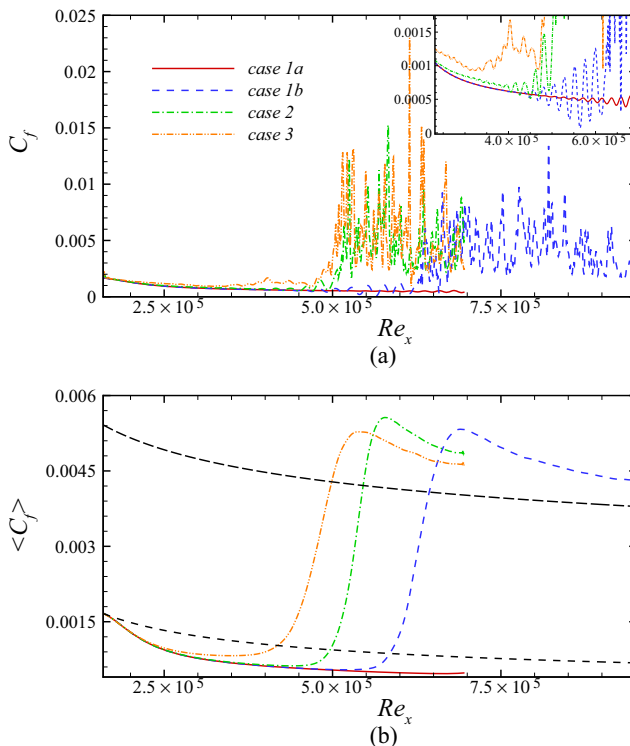


FIG. 7. (a) Instantaneous skin-friction coefficient (C_f) at a select spanwise location plotted against Re_x for all cases tabulated in Table I. An enlarged view of the curves is shown in the inset. (b) Mean skin-friction coefficient ($\langle C_f \rangle$) plotted against Re_x . The line type and color for individual cases are the same as in Fig. 7(a). The black dashed lines represent the laminar solution and turbulent correlation.

edge. x_1 is obtained by equating δ_0 to the 99% thickness of the APG boundary layer ($\beta_H = -0.14$) at the inlet Reynolds number. In the inset of Fig. 7(a) is an enlarged view; the presence of instability waves for all cases is clear. The magnitude of instability waves is highest for the case 1b.

Streaks are the boundary-layer response to free-stream forcing, at intensities $Tu \geq 0.5\%$. Hence cases with $Tu \geq 0.5\%$ can potentially undergo mixed-mode transition. There is significant difference in the transition routes undertaken in such cases.

In Fig. 7(b), the mean skin-friction coefficient $\langle C_f \rangle$ is plotted versus Re_x . The flow remains laminar within the computational domain for the very low intensity case ($Tu = 0.1\%$) simulated in shorter domain (case 1a). That is why the large domain case (case 1b) was simulated. Case 1b transitions within its computational domain. Despite their matching free-stream forcing intensities, cases 1a and 1b have drastically different instability routes. The difference is due to their spectra at the inlet.

Reynolds numbers and streamwise locations of transition inception and completion for all cases are listed in Table II. The onset of transition is defined as the location where $\langle C_f \rangle$ is minimum in Fig. 7(b). Similarly, completion of transition is the location where $\langle C_f \rangle$ is maximum.

A. Effect of inlet FST spectrum on transition location

The difference in the spectra of the inlet disturbances has a profound effect for cases 1a and 1b. These two cases are first compared phenomenologically by plotting the perturbation velocity fields. In Fig. 8, contours of u' are shown at different wall-normal heights for case 1a. The free-stream

TABLE II. Transition onset and completion locations for all cases.

Case	Transition onset		Transition completion	
	Re_x	x_s	Re_x	x_e
1a				
1b	5.2×10^5	211.25	6.9×10^5	316.5
2	4.4×10^5	163.75	5.8×10^5	247.5
3	3.5×10^5	109.3	5.4×10^5	224.3

disturbances have many scales. In the horizontal plane at $y = \delta_0$, up to some distance downstream of the inlet, broadband disturbances persist. When this plane is sufficiently inside the boundary layer, after $x \sim 80$, streaky disturbances appear. Further downstream, in the last quarter of the domain, locally spanwise coherent instability waves start to amplify. Those are clearly modulated by the streaks. Deep inside the boundary layer, shown in the bottom frame, streaks are much weaker; by the exit plane instability waves dominate the flow field. At the exit plane, the 99% boundary-layer thickness is at $y = 2.59\delta_0$. The selected plane shown in the bottom frame is below the critical layer of the instability waves.

Transition takes place in case 1b. Figure 9 shows the u' and v' contours at $y = \delta_0/2$ for this case. There is significant difference between u' in the top frame and the bottom frame of Fig. 8 for case 1a, at the same wall-normal height. The instability waves are prominent, although their wavelength changes as the flow moves downstream. This change is seen clearly in the v' plot (bottom frame of Fig. 9). Three separate zones are identifiable. Just downstream of the inflow plane, marked as zone i in the bottom frame, the wavelength is shorter than the waves in zone iii , prior to transition. In between, in zone ii , a change in wavelength takes place. Transition is triggered by breakdown of the newly dominant instability wave.

The rms of u' and v' are plotted in Fig. 10 at a constant wall-normal height, $y = 0.7\delta_0$. This fixed location is chosen because the peak rms values for a portion of that plane, close to the inlet, are in the free stream. This wall-normal height corresponds to $y \sim \delta_{99}/3$ in the transitional regime. For both cases 1a and 1b, there is some weak, initial growth of the u perturbation, followed by viscous decay. For both cases, u'_{rms} grows again from $x \approx 25$; the growth is exponential, as the curves are linear, when plotted on a logarithmic scale. For case 1b, v' amplifies and, from $x \approx 110$, grows all

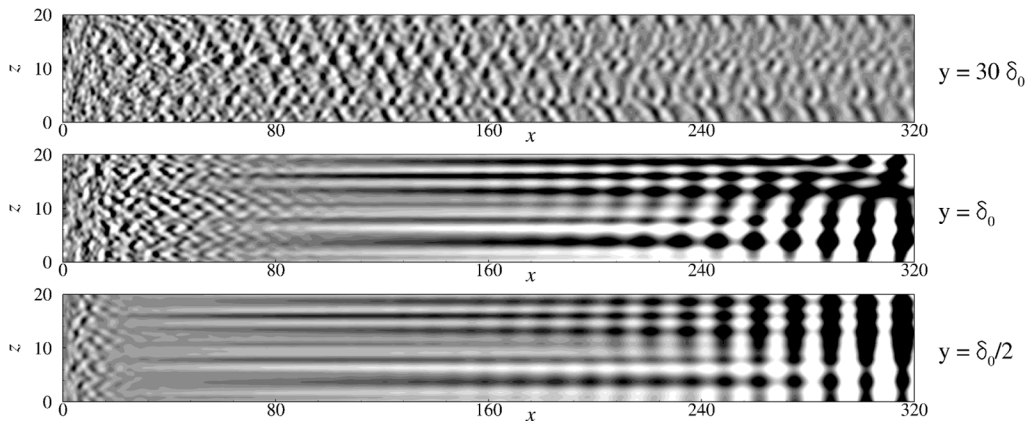


FIG. 8. Instantaneous contours of $-0.001 \leq u' \leq 0.001$ in x - z planes at indicated wall-normal heights for case 1a. The z axis has been enlarged by a factor of two. Dark contours represent negative values.

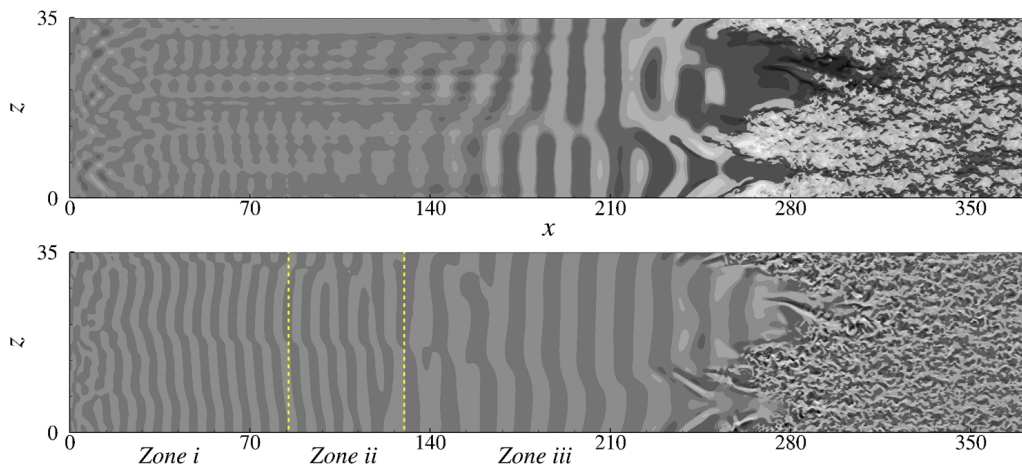


FIG. 9. Instantaneous contours of $-0.4 \leq u' \leq 0.4$ (top frame) and $-0.2 \leq v' \leq 0.2$ (bottom frame) at a wall-normal height $y = \delta_0/2$ for the case 1b. The z axis has been enlarged by a factor of two. Dark is negative.

the way to transition. The disturbance rms for case 1a increases at a lower rate. The change in the rate of amplification is due to a change in the dominant instability wave.

1. Primary instability

The most dominant instability wave is identified by plotting the frequency spectra of v' for cases 1a and 1b in Fig. 11. A few inlet disturbance frequencies are also marked by squares, in the figure. Only frequencies with at least 16 periods in the stored time series are plotted. The spectra are broadband, and dominated by disturbances with frequencies lower than the smallest inlet frequency. Hence, they are created by fluid mechanics, within the computational domain.

Clearly, the most dominant frequencies differ for the two cases. The dominant frequency for case 1a is $\omega = 0.17$. The 2D modes corresponding to this frequency show up in the contour plots in Fig. 8.

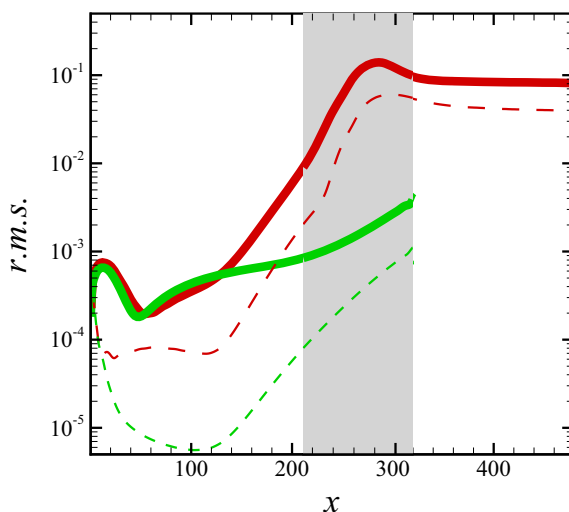


FIG. 10. u'_{rms} (thick solid) and v'_{rms} (thin dashed) as a function of x at a wall-normal height $y = 0.7\delta_0$ for the cases 1a (green) and 1b (red). The shaded portion is the transitional regime for case 1b.

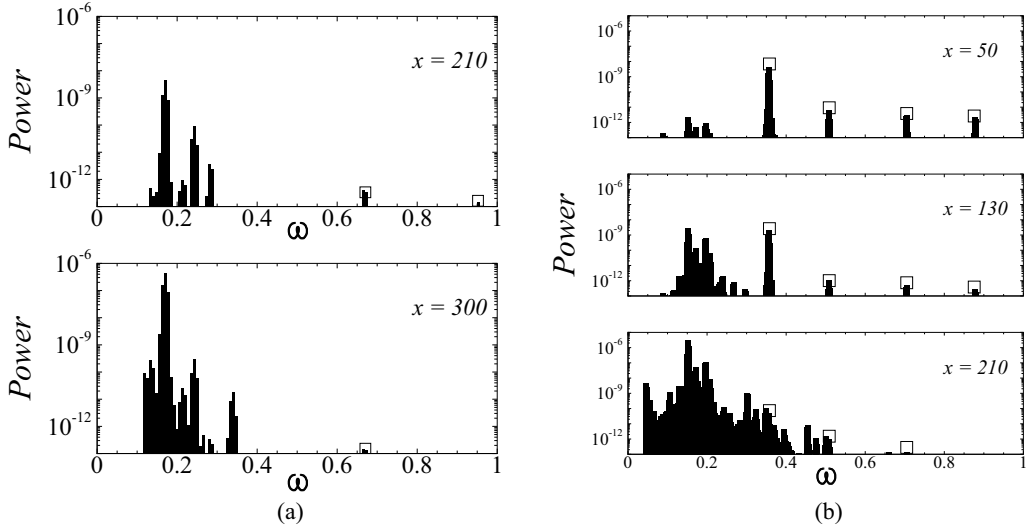


FIG. 11. (a) Frequency spectra of v' for cases (a) 1a and (b) 1b. For case 1a, the wall-normal location is at $y/\delta_{99} \sim 0.33$. For case 1b, the locations at $x = \{50, 130, 210\}$ are to $y/\delta_{99} = \{0.51, 0.4, 0.33\}$. Black squares mark frequencies that are prescribed at the inlet.

At this frequency, the most unstable wavelength is $13.08\delta_0$ as per linear spatial stability theory. The average wavelength of disturbances from DNS at $x = 210$ is $13.44\delta_0$.

Figure 11(b) helps to identify the most unstable frequencies for case 1b. To aid the interpretation of the spectra, contours of the locally most unstable eigenvalues (k_i) from the OS equation for the DNS mean flow are plotted in Fig. 12(a). The lowest frequency excited at the inlet is $\omega = 0.357$ which has the maximum amplitude at $x = 50$ in Fig. 11(b). $\omega = 0.357$ is unstable up to $x \approx 91$ [Fig. 12(a)].

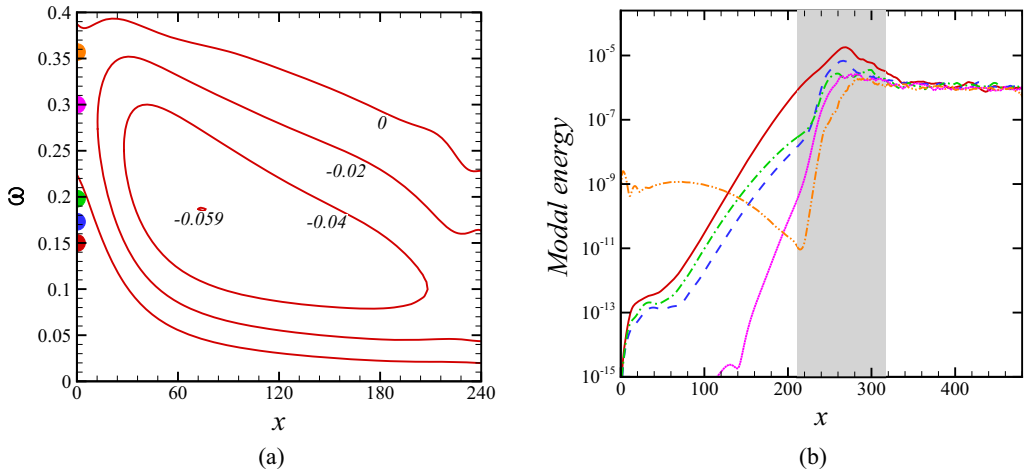


FIG. 12. (a) Contours of the linear spatial growth rate (k_i) plotted in (x, ω) plane for case 1b. The frequency peaks indicated in Fig. 11(b) are also marked on the ω axis. (b) Downstream amplification of v' perturbation energy at dominant frequencies from the spectra in Fig. 11(b): $\omega = 0.15$ (solid red), $\omega = 0.173$ (dashed blue), $\omega = 0.198$ (dash-dotted green), $\omega = 0.3$ (dotted pink), and $\omega = 0.357$ (dash-dot-dotted orange). The transition regime is marked by the vertical gray strip.

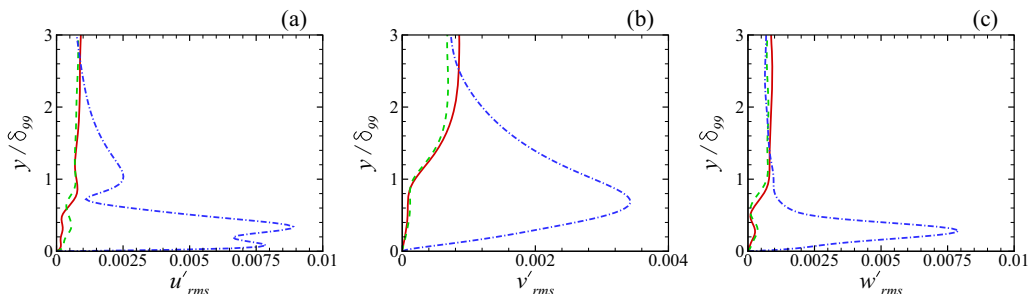


FIG. 13. Mean rms perturbation velocity profiles plotted at selected streamwise stations for the case 1b at streamwise stations: $x = 50$ (solid red), $x = 130$ (dashed green) and $x = 210$ (dash dotted blue).

As the flow develops downstream, the frequency of the most unstable mode decreases. The most dominant frequency at $x = 210$ is $\omega = 0.15$ [Fig. 11(b)] which only starts amplifying at about $x = 16$ as per linear theory. So, for $x > 91$, disturbances with frequencies $\omega = \{0.15, 0.174, 0.198\}$ start amplifying at a high rate while $\omega = 0.357$ starts decaying [also see Fig. 12(b)].

Amplification of v' disturbances at the aforementioned frequencies is shown by plotting the modal energy ($\hat{v}\hat{v}^*$) versus streamwise stations in Fig. 12(b). Clearly, $\omega = 0.357$ has a much higher amplitude at the inlet. From $x \sim 30$, disturbances with $\omega = \{0.15, 0.173, 0.198\}$ start growing at an exponential rate. It is interesting to note that $\omega = \{0.15, 0.198, 0.357\}$ form a triad. Perhaps, 2D disturbances with $\omega = 0.15$ eventually dominate due to nonlinear energy transfer to this frequency [28]. The energy for $\omega = 0.15$ overtakes that for $\omega = 0.357$ at $x \sim 128$ and becomes the most dominant instability wave which eventually breaks down to turbulence (Fig. 9).

The wavelength predicted by linear theory for the most unstable mode at $x = 50$ with frequency $\omega = 0.357$ is $6.8\delta_0$. The average wavelength of disturbances from DNS at this location is approximately $6.9\delta_0$ (zone *i* in Fig. 9). The most unstable mode at $x = 210$ (zone *iii*) has frequency $\omega = 0.15$ and wavelength $13.9\delta_0$; the average wavelength observed from DNS is approximately $13.6\delta_0$.

It is important to note that the change in transition from case 1a to case 1b is not due to a change in the primary instability of the base flow and its eigenspectrum; the mean flows from these calculations were the same until secondary instability kicked in for case 1b. Instead, it is due to the change in the spectrum of the free-stream disturbance, which interacts with the boundary layer and seeds its primary instability.

2. Transition to turbulence: Λ vortices

The critical layer of the instability waves is closer to the wall (often at $y/\delta_{99} \sim 1/3$). Disturbance amplification is expected to be most prominent near that location [28]. Profiles of rms perturbations for all three velocity components are plotted in Fig. 13. The ordinate is the wall-normal distance scaled by the local 99% boundary-layer thickness. The selected streamwise stations are the same as in the spectra of Fig. 11(b) (representative of each zone in Fig. 9). A clear peak inside the boundary layer is only noted at $x = 130$ for all the velocity components. Disturbance amplification is appreciable for $50 < x < 130$ and comparatively much higher between $x = 130$ and $x = 210$ due to the high exponential amplification rate in zone *iii* [see Fig. 12(a)]. All three velocity perturbation components are of the same order of magnitude in the transitional regime. In fact, the peak wall-normal rms of u and w is almost the same at the onset of transition, at $x = 210$. In a purely bypass transitional boundary layer, the u perturbation is generally three to five times larger than the other two components [23]. Here the transition process is more akin to orderly breakdown.

The late stages of orderly transition are well documented [17,18]. The three-dimensional secondary instability leads to the formation and breakdown of Λ -shaped vortices. Although there is an idealized notion of K- and H-type patterns—fundamental or subharmonic secondary instabilities

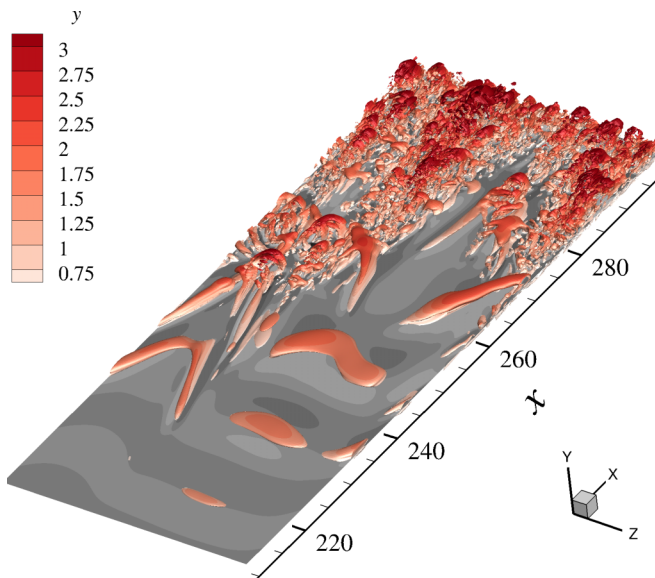


FIG. 14. Isosurfaces of the Q criterion colored by the wall-normal distance y for the case 1b. Here, $Q = 0.003$. Also shown are the contours of $-0.3 \leq v' \leq 0.3$ in a horizontal plane at a wall-normal height $y = 0.7\delta_0$. Dark is negative. δ_{99} at $x = 250$ is at $y = 2.33$.

of the primary wave, appearing as Λ vortices arrayed either as aligned or staggered patterns—in a broadband disturbance environment those patterns do not occur. For example, Borodulin *et al.* [29,30] investigated natural transition in a Falkner-Skan boundary layer ($\beta_H = -0.115$). A monochromatic instability wave was perturbed by broadband disturbances through wall excitation. Transition to turbulence was via Λ vortices with various shapes, sizes and alignments. The transition process for case 1b is qualitatively similar to these observations. However, in the present case, the primary instability appears spontaneously and is not monochromatic.

Isosurfaces of the Q criterion are shown in Fig. 14, colored by the wall-normal distance y . A horizontal slice at $y = 0.7\delta_0$ with contours of v' is also included. Vortices are manifest at the junction of negative and positive patches of v' , implying the 2D vortices have negative vorticity. The Λ vortices break down at their tips to spawn patches of turbulence. A fully developed Λ structure is seen to break down at the far end, $x \sim 250$. The tips of fully formed Λ vortices extend to the boundary-layer edge. Occasionally, these vortical structures start breaking down before being fully formed, for example, in the middle of the domain near $x \sim 265$. Also, unlike Λ vortices generated by monochromatic forcing, the vortices in the present simulation are often asymmetric, being tilted toward one side or the other [29]. The spanwise sizes of these vortices vary between 9 and $15\delta_0$. Herbert [31] predicted a range of spanwise wave number, b , using Floquet stability theory for significant subharmonic secondary growth in ZPG boundary layer. The highest amplification was obtained for $b \sim 0.2$. The nondimensional spanwise wave number for a Λ vortex of size $12\delta_0$ is $b \approx 0.68$. Hence, the vortices observed here are quite wider than those of H- and K-type secondary instability.

Temporal evolution of the pattern of Λ vortices is not strictly periodic. This is demonstrated by plotting the contours of u' in the (t, z) plane at $x = 250$ in Fig. 15(a). The local profile of u'_{rms} is plotted in Fig. 15(b) at this streamwise position to show the wall-normal location of data-extraction relative to the boundary-layer thickness and the disturbance peak. An apparent row of Λ vortices aligned in the streamwise direction with their apex at $z \sim 5$ is seen. But if closely examined, their streamwise alignment is not exact and the vortices are at varying stages of development from time to time. The fluctuating contour values and their distortion reveal the asymmetric nature of the vortices. Often a few vortices merge together to form more complex structures [29], e.g., the vortices between

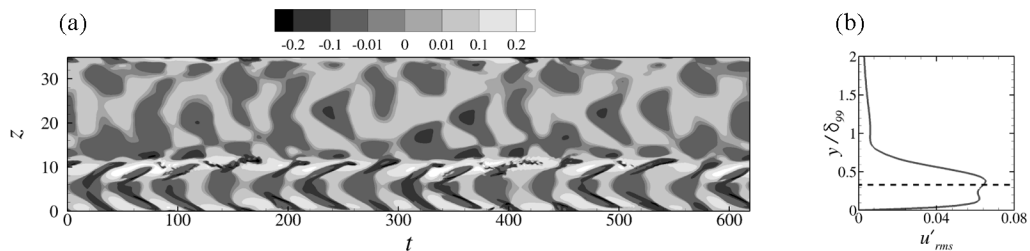


FIG. 15. (a) Contours of $-0.2 \leq u' \leq 0.2$ in the (t, z) plane for the case 1b. The streamwise station is $(x = 250, y = 0.775)$. (b) Profile of u'_{rms} at $x = 250$. The dashed line indicates the wall-normal location of the station corresponding to panel (a).

$t = 300$ and 400 . The evolution depends on the instantaneous disturbances within the boundary layer and the forcing from the free stream.

B. Effect of inlet FST amplitude on transition

The inlet disturbance spectra for cases 2 and 3 in Table I are a scaled version of that for case 1a. The only difference is the amplitude, or Tu . For both cases, transition is triggered and its location is earlier upstream with increasing levels of FST (Fig. 7).

1. Primary instability

Instantaneous contours of u' and v' are plotted in Fig. 16 for case 2. The selected horizontal planes are at the wall-normal height where u'_{rms} has its local peak at the onset of transition. Unlike the very low Tu cases 1a and 1b, visual identification of the primary instability is not straightforward. On one hand, the streamwise Klebanoff streaks are apparent in the u' contours; on the other, the two-dimensional instability waves are clearly identifiable in the v' contours. As in pure bypass transition, v' perturbations are initially associated with the low-frequency Klebanoff streaks. Downstream, from $x \sim 80$ onward, the instability waves seem to take over and become dominant. In APG, the Klebanoff streaks and instability waves have competing growth rates. From Fig. 16, it is difficult to ascribe breakdown to bypass transition (top frame) or to instability waves (bottom frame) conclusively. Such transitional flow is complex, and best described as a *mixed-mode* regime [10].

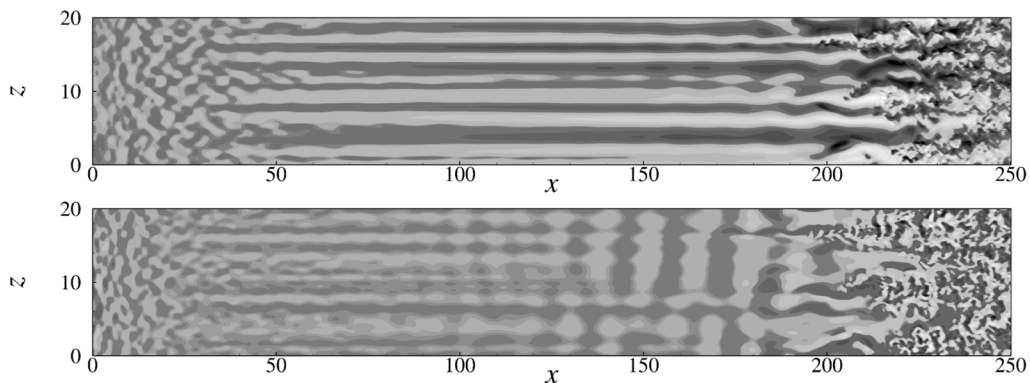


FIG. 16. Instantaneous contours of $-0.3 \leq u' \leq 0.3$ (top frame) and $-0.2 \leq v' \leq 0.2$ (bottom frame) at a wall-normal height $y = 0.87\delta_0$ for the case 2. Dark is negative. Local peak of u'_{rms} is at this wall-normal height at transition onset.

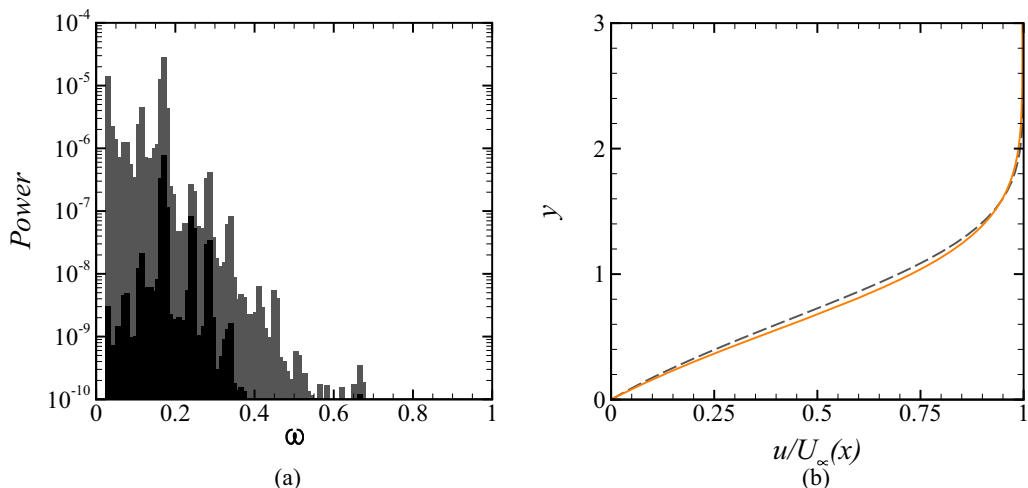


FIG. 17. (a) Frequency spectra of u' (gray) and v' (black) for the case 2 at $x = 155$. The wall-normal location is $y/\delta_{99} \sim 0.285$. (b) Comparison of mean streamwise velocity profiles for cases 1a (black dashed line) and case 2 (orange solid line) at $x = 155$.

To identify the primary instability for case 2, the frequency spectra of u' and v' components are shown in Fig. 17(a) at $x = 155$, just upstream of onset of transition (see Table II). The spectrum is evaluated at a height $y \sim 0.285\delta_{99}$ from the wall. The time span of the data equals 16 periods of the lowest frequency in the spectrum. The linearly unstable modes for the time-averaged flow from the DNS at this station are in the range $\omega \in [0.031, 0.266]$. This range is much higher than the streaky perturbations in Fig. 16. The most dominant frequency in the spectrum is $\omega = 0.17$ and is therefore within the range predicted by linear theory. The instability waves are more prominent in the spectrum for v' compared to u' , but the same peaks can be identified in both quantities. Also prominent in the spectrum for u' is the peak at very low frequencies due to Klebanoff streaks.

Interestingly, the dominant instability wave is the same as the dominant mode in case 1a. As noted earlier, the inlet spectra for these two cases are similar except the amplitude scaling. In Fig. 17(b), local profiles of the scaled mean streamwise velocity (u/U_∞) are plotted for cases 1a and 2 at the streamwise station where the spectra were computed. There is some difference between the profiles from the two cases. The results reaffirm the influence of the inlet spectrum on the most dominant instability waves and transition in APG, even at moderate Tu .

Disturbance energy in u' and v' perturbations at the most energetic frequency $\omega = 0.17$ and the lowest frequency in the spectra, $\omega = 0.0077$, are plotted as functions of x in Fig. 18. The energy of the lower frequency mode is included to compare the growth rates of the instability wave (at $\omega = 0.17$, dash dotted lines) and Klebanoff streaks (at $\omega = 0.0077$, solid lines). Thick (blue) and thin (red) lines represent the mode energy for u and v components, respectively. As expected, the lower frequency amplifies more quickly. Also the transient amplification is more pronounced for u' . The amplitude of u' is at least three orders of magnitude higher than v' as the disturbances saturate. On the other hand, the disturbance with $\omega = 0.17$ amplifies exponentially for both u' and v' from $x \sim 80$ onward. In the transitional region, demarcated by the gray strip, the disturbances with $\omega = 0.17$ are about the same order of magnitude as $\omega = 0.0077$. Exponentially growing waves thus contribute appreciably during the transition process.

The instability wave role in transition to turbulence is less clearcut at higher FST levels (case 3). Evidence suggests that the TS waves are excited, but streaks become more dominant. Contours of instantaneous u' and v' are plotted in a horizontal plane that slices through the boundary layer in Fig. 19. The FST intensity is 2% at the inlet. Only long-wavelength streamwise streaks are detectable

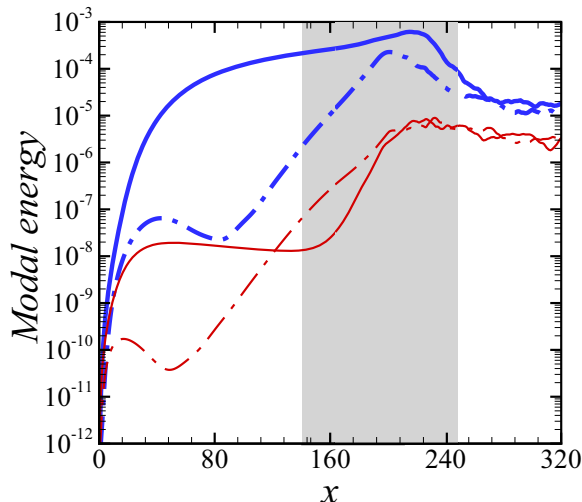


FIG. 18. Downstream amplification of perturbation energy in u' and v' at dominant frequencies from frequency spectra for the case 2 in Fig. 17(a): $\omega = 0.0077$ (solid), $\omega = 0.17$ (dash-dotted). Thick (blue) and thin (red) lines indicate the mode energy for u and v components, respectively. Onset and completion of transition is distinguished by the vertical gray strip.

in the u' contour plot in the top frame. The v' contours in the bottom frame qualitatively resemble the u' contours, but spanwise coherent patches can be identified in v' from $x \sim 120$ onward.

Frequency spectra for u' and v' perturbations are plotted in Fig. 20(a) at $x = 130$ for case 3, just after the onset of transition (Table II). Also included is the frequency spectrum for v' with spanwise wave number $k_z = 0$, i.e., for 2D disturbances. The selected point is at $y \sim 0.267\delta_{99}$, close to the critical layer of instability waves. The range of frequencies for linear instability of the base profile is marked by the gray strip. A broadband peak, at lower frequencies than the exponentially unstable range, is seen for the u component. Similar to case 2, the peak in the v' spectrum is highest in the frequency range of exponential instability. At higher frequencies, such as $\omega = \{0.17, 0.243, 0.285\}$, the 2D instability waves have almost the same magnitude as the overall spectrum.

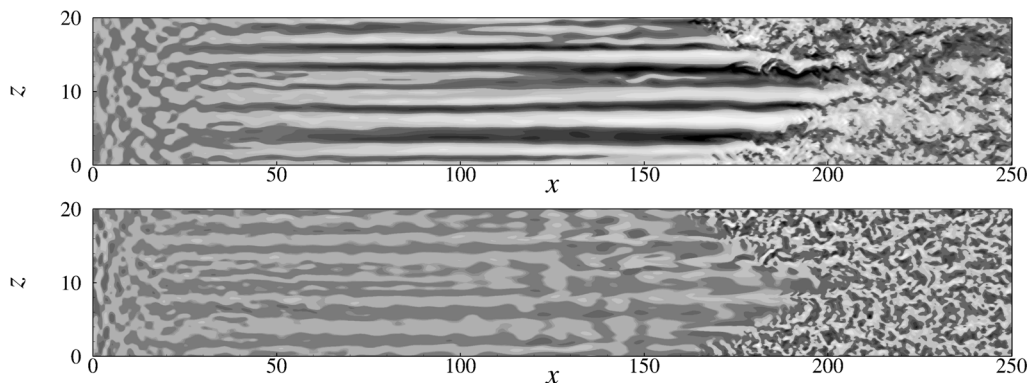


FIG. 19. Instantaneous contours of $-0.3 \leq u' \leq 0.3$ (top frame) and $-0.2 \leq v' \leq 0.2$ (bottom frame) at a wall-normal height $y = 0.75\delta_0$ for the case 3. Dark is negative. The wall-normal peak of u'_{rms} is at $y = 0.75\delta_0$ at transition onset.

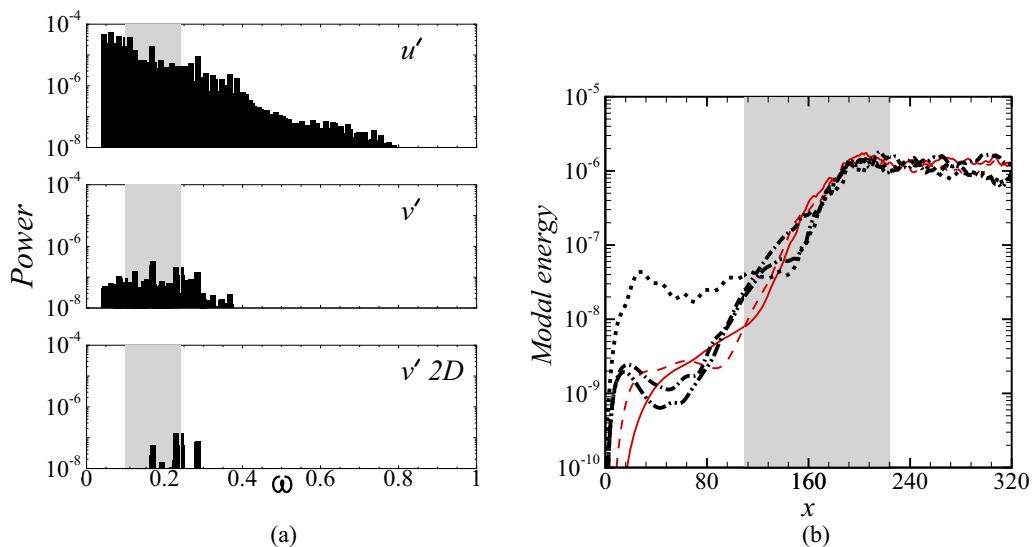


FIG. 20. (a) Frequency spectra of u' , v' , and 2D component of v' for the case 3 at $x = 130$. The wall-normal location corresponds to $y/\delta_{99} \sim 0.267$. The gray region shows the exponentially unstable frequency range for the mean velocity profile. (b) Downstream amplification of perturbation energy in v' at dominant frequencies from spectra plot in Fig. 20(a): $\omega = 0.083$ (solid), $\omega = 0.114$ (dashed), $\omega = 0.17$ (dash-dotted), $\omega = 0.243$ (dash-dot-dotted), and $\omega = 0.285$ (dotted). The black lines represent frequencies dominated by 2D modes. Onset and completion of transition is highlighted by the vertical ash-colored strip.

Downstream amplification of v' disturbances at selected frequencies are shown in Fig. 20(b). Amplification of frequencies dominated by two-dimensional disturbances are coloured black. After an initial transient amplification, all frequencies grow exponentially up to the transition region marked by the gray strip. Disturbance energy is similar for all the shown frequencies in this region. Downstream, the secondary instability of streaks and their breakdown to turbulence are triggered by high-frequency disturbances, which are largely due to two-dimensional instability waves.

2. Secondary instability: Inner and outer modes

The discrete instability waves are excited spontaneously under APG conditions, as evidenced by the perturbation spectra, but their presence is masked by the Klebanoff distortions at moderate and high Tu. In cases 2 and 3, the streamwise streaks locally break down due to secondary instabilities and form turbulent spots. The secondary disturbances can be classified into “inner” and “outer” modes based on the heights of their critical layers [20]. Previous works include the studies by Cossu and Brandt [8] and Liu *et al.* [32]. They performed Floquet stability analysis of periodic base flows that included both the Klebanoff streaks (steady) and an instability wave, albeit in ZPG boundary layer. Hack and Zaki [21] performed linear secondary stability analysis of velocity fields extracted from DNS of bypass transition in APG and were able to take into account the inherently local nature of the secondary instabilities. They found the critical layer of secondary instability in APG to be closer to the wall compared to ZPG. Similar observations are made from the present results. The discussion is solely based on analysis and visualization of mean and disturbance flow fields from the present DNS.

Wall-normal profiles of rms perturbations at select streamwise positions are plotted in Figs. 21 and 22 for cases 2 and 3, respectively. A wall-normal peak for u perturbations is obtained at all stations considered while peaks in v and w perturbations are only obtained well downstream of the inlet. This is due to transient amplification of u' . The peaks for all the components are within $y/\delta_{99} < 0.5$, which is an indicator of the deep lying critical layer: for case 2, the peak of u'_{rms} is at $y/\delta_{99} \sim 0.45$

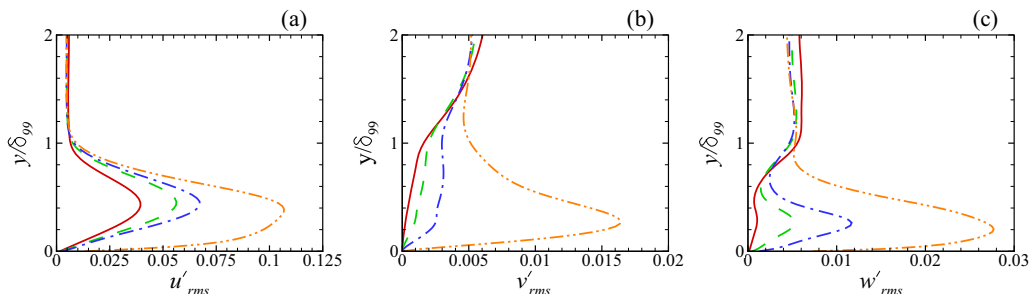


FIG. 21. Mean rms perturbation velocity profiles plotted at selected streamwise stations for the case 2 at streamwise stations: $x = 100$ (solid red), $x = 150$ (dashed green), $x = 175$ (dash-dotted blue), and $x = 200$ (dash-dot-dotted orange).

and for case 3 it is at $y/\delta_{99} \sim 0.4$. Also, the peaks for v and w profiles are closer to the wall than the u component. This difference is because the Klebanoff streaks contribute mainly to u' .

As for the transitional case 1b, the rms amplitudes of v' and w' are of the same order of magnitude as u' for case 2. This behavior is characteristic of transition by discrete instability waves. Because of the very high growth rate of the instability, v' grows quickly in APG. With the additional presence of the streaks, the flow configuration becomes one of *mixed mode* transition. On the other hand, for case 3, peak rms of u' is at least an order of magnitude higher than the v' and w' , which indicates that this case is more in line with the conventional bypass transition dominated by Klebanoff streaks.

The flow structures in an APG transitional boundary layer are different from their ZPG counterpart. While bypass transition in ZPG is dominated by outer sinuous instabilities, inner instabilities are prevalent in APG [23,33]. Secondary instability and consequent breakdown for case 2 are initiated via the secondary helical modes [34], which are essentially a class of inner modes. Helical features are seen in both cases 2 and 3, but more frequently identifiable for case 2. In Fig. 23(a), an emergent helical mode breakdown is shown by isosurfaces of $u' = -0.15$. It develops on a negative streak, in the high shear region between adjacent positive and negative streaks. Hack and Zaki [21] found that inner secondary instabilities develop in similar high shear regions. Bose and Durbin [34] attributed the helical breakdown to interaction of instability waves and Klebanoff streaks.

The streaks are jetlike, streamwise perturbations; these may be assumed to be the primary state. The helices are flow structures observed in u' isosurfaces. Therefore, these may be termed secondary perturbations. Following the analysis by Hack and Zaki [21], therefore, streamwise vorticity (ω_x)

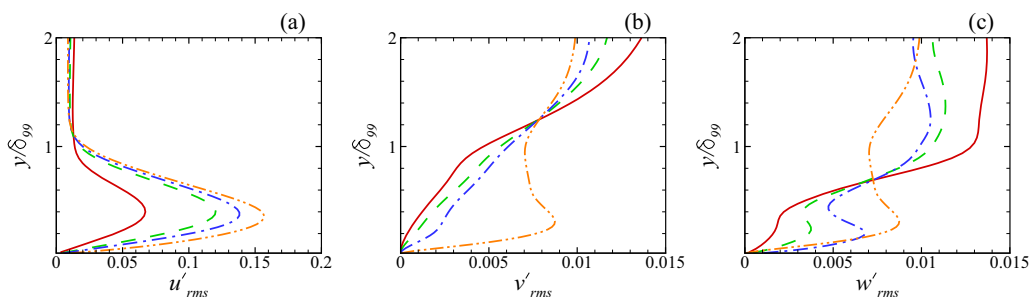


FIG. 22. Mean rms perturbation velocity profiles plotted at selected streamwise stations for the case 2 at streamwise stations: $x = 50$ (solid red), $x = 100$ (dashed green), $x = 125$ (dash-dotted blue), and $x = 150$ (dash-dot-dotted orange).

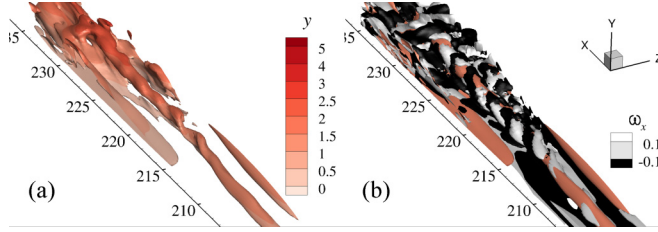


FIG. 23. (a) Isosurfaces of $u' = -0.15$ colored by the wall-normal distance y showing a helical secondary instability for case 2 [24]. (b) Isosurfaces of streamwise vorticity $\omega_x = \pm 0.1$ are overlaid on the helix. The boundary layer thickness at $x = 215$ is $\delta_{99} = 2.26\delta_0$.

approximately represents the secondary disturbances:

$$\omega_x = \bar{\omega}_x + \omega_x^p + \omega_x^s.$$

Here, three terms on the right-hand side are streamwise vorticity due to mean flow, primary perturbations, and secondary perturbations, respectively. $\bar{\omega}_x = 0$ for the mean flow, and $\omega_x^p \approx 0$ for the primary disturbances which are streaks, predominantly u' . So, $\omega_x \approx \omega_x^s$, where ω_x^s denotes the streamwise vorticity due to secondary perturbations. Isosurfaces of ω_x for a pair of positive and negative values are plotted in Fig. 23(b) that depict the helical nature of the instability. Isosurfaces of $u' = -0.15$ are also shown. Prior to formation of the helical mode, isosurfaces of ω_x wrap around the unstable streak. Initially ω_x is weak and strengthens with formation of the helical instability.

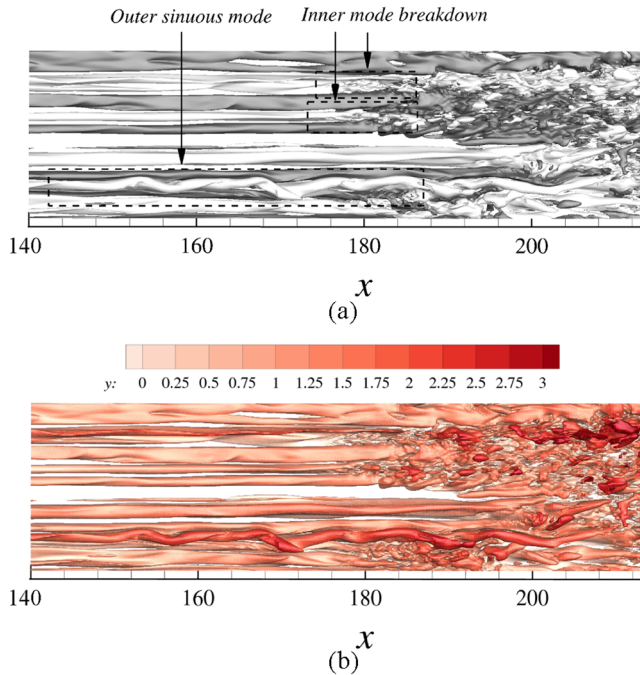


FIG. 24. Instantaneous isosurfaces of $u' = \pm 0.1$ depicting inner mode breakdown and outer sinuous mode spot precursor for the case 3: (a) $u' = 0.1$ (dark) and $u' = -0.1$ (gray), and (b) color contoured by the wall-normal distance y . Boundary layer thickness at $x = 155$ is $\delta_{99} = 2.28\delta_0$.

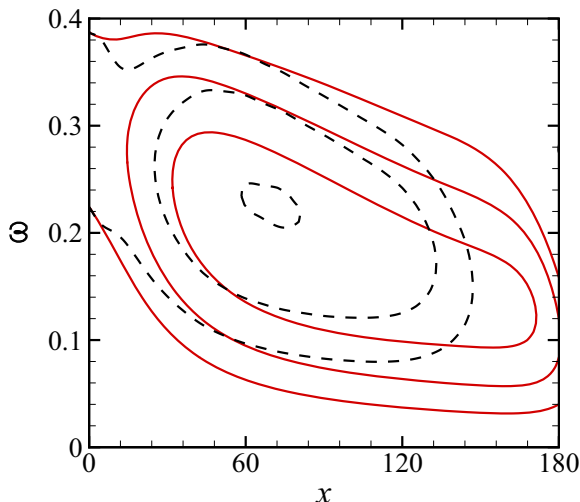


FIG. 25. Contours of spatial growth rate (k_i) plotted in the (x, ω) plane as per linear stability theory for the time- and span-averaged mean flow for cases 2 (red solid) and 3 (black dashed). Contour levels are between 0 and -0.04 with step size -0.02 . Minimum k_i was -0.056 for case 2 and -0.04 for case 3.

After inception of the secondary instability, the isosurfaces of ω_x orient in an approximately helical pattern. For $x > 215$, troughs and crests in ω_x become apparent along the helical structure.

Flow structures for case 3 are more diverse. Both inner and outer secondary instabilities are observed. In Fig. 24(a), isosurfaces of u' are plotted for selected values to visualize breakdown of streaks at an instant. Breakdown of two separate inner modes is captured. At the same time, an outer sinuous mode, also, is developing prior to its breakdown. In Fig. 24(b), those same isosurfaces are colored by wall-normal distance y to highlight the wall-normal location of the streaks. That the outer mode grows on a low-speed streak is evident. The streamwise extent of the instability prior to the onset of turbulence is long. The inner mode breakdowns take place on streaks closer to the wall, which is clear from Fig. 24(b), and the onset of turbulence is abrupt.

For case 2, the inner modes are the only breakdown route; outer modes are entirely absent. A relative measure of inner and outer breakdowns was noted by following flow structures prior to their breakdown, in animations of disturbance velocity fields created from instantaneous snapshots of DNS data at regular time intervals. A total of 22 breakdown sequences were observed within a time span of $491.4 \frac{\delta_0}{U_0}$ for case 2. All the breakdowns were via inner instabilities. For 21 of these spot precursors, the noted streamwise wavelength was between $2\delta_0$ and $3\delta_0$. The exceptional inner spot precursor had a wavelength of $5\delta_0$. Phase speed of these inner forerunners ranged between $0.31U_0$ and $0.55U_0$.

For the higher Tu case 3, the outer modes are sparsely seen while the dominant mode is still the inner mode. The time span for analysis for case 3 was $561.6 \frac{\delta_0}{U_0}$, within which 12 breakdowns were observed. Three of these 12 breakdowns were preceded by a long outer instability with wavelength in the range $8\delta_0$ – $10\delta_0$ and phase speed $\sim 0.75U_0$. The other nine spot precursors had phase speed in the range $0.4U_0$ – $0.6U_0$. Two of these nine inner instabilities had wavelength comparable to outer modes ($\sim 8\delta_0$) which also had higher phase speed ($\sim 0.6U_0$). Off the seven remaining inner breakdowns, four had dispersion relation similar to helical instabilities (wavelength $2\delta_0$ – $3\delta_0$ and phase speed $\sim 0.5U_0$). The wavelength of the other three forerunners could not be determined.

The dominance of the secondary inner modes in APG might be attributed to the inflectional base profile [21]. To justify that argument, spatial growth rates (k_i) of the most unstable eigenvalue of the Orr-Sommerfeld (OS) equation are plotted in the (x, ω) plane for the cases 2 and 3 in Fig. 25. The flow field used for the calculation is the time- and span-averaged mean flow from DNS. The

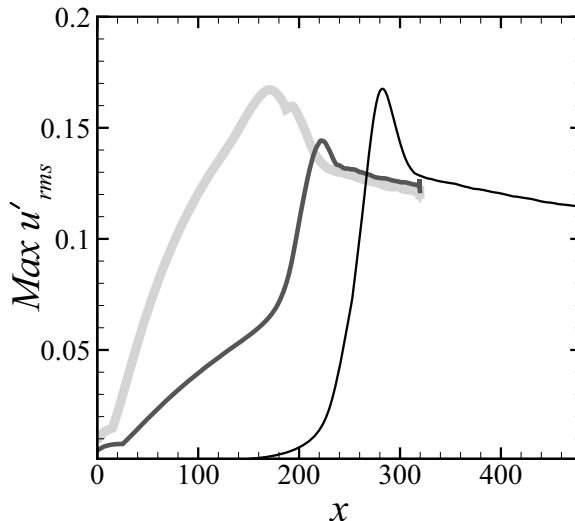


FIG. 26. Local peak u'_{rms} plotted vs streamwise distance x for cases 1b (dark), 2 (gray), and 3 (light).

minimum $k_i = -0.056$ for the case 2. Also, Fig. 25 shows an extended region of high exponential amplification.

The outer-mode breakdowns in APG are more frequent at high $Tu = 2\%$, which is case 3. Two considerations contribute to the change in flow stability. First, high-amplitude Klebanoff streaks are subjected to high-frequency forcing from the free stream, enhancing secondary instability. Figure 26 shows the local peak u'_{rms} as a function of x for all the transitional cases reported here. Streamwise disturbance magnitude reaches a higher value in case 3 than case 2, prior to transition. Second, the finite-amplitude Klebanoff streaks indirectly affect stability of the mean flow; they distort the base flow to make the inflectional profile to fuller [35], and therefore, less unstable. The effect is more pronounced for higher amplitude Klebanoff streaks. Consequently the growth rate of the linear instability waves is decreased. The minimum value of k_i for the case 3 is -0.04 in Fig. 25.

These arguments based on flow structures from DNS at moderate Tu are consistent with a statistical study by Hack and Zaki [21]. They reported about 65% breakdowns in APG bypass transitional boundary layer are preceded by inner instabilities at a higher $Tu = 3\%$. It must also be noted that even though their APG level was same as the present study, their inlet Reynolds number was subcritical while the present study focused on supercritical conditions.

IV. CONCLUSION

The role of instability waves in adverse pressure gradient (APG) boundary layer transition beneath free-stream turbulence (FST) was investigated by means of direct simulations. It has been seen that instability waves contribute to transition, even with free-stream turbulence intensities of 2%. The present results are all for a Falkner-Skan boundary layer. The pressure gradient and inlet Reynolds number are sufficiently high ($\beta_H = -0.14$, $Re_b = 400$) so that exponentially growing instability waves are spontaneously aroused even in the calculation without FST. When FST was introduced at the inlet, the instability waves were detected for all the cases considered. The spectral makeup of the turbulence in the free stream is as important as its intensity in dictating the instability and transition route. This was demonstrated by considering two cases with the same low intensity ($Tu = 0.1\%$), but with different spectral content. Neither included the wave-number–frequency combination of the linear exponential instability waves. Yet, of the two spectra, transition was only triggered for case 1b, which contained the frequency (but not wave number) of an unstable, instability wave.

The most dominant primary instability changes with streamwise distance, depending on modal energy (Fig. 9). The spectrum prior to development of secondary instability is, therefore, broadband. For low-intensity FST at inlet ($Tu = 0.1\%$), the flow undergoes transition via secondary instability of the primary waves. Those take the form of Λ vortices with irregular structures and patterns due to the broadband forcing from the free stream (Fig. 15).

The effect of free-stream forcing amplitude was studied by increasing Tu but keeping the inlet turbulent scales unchanged. The most dominant instability waves remain the same from case to case (cases 1a, 2, and 3). At $Tu = 1\%$ (case 2), instability waves are clearly identifiable in the transitional region in u and v perturbation contours and instantaneous skin-friction plots. Perturbation velocity spectra reveal that the instability waves are dominant in both u' and v' and are only masked by the Klebanoff streaks in the former. The dominant 2D instability wave frequency has the highest magnitude in the nonlinear transitional region; disturbances at this frequency grow exponentially, even in this region. Breakdown to turbulence is via flow structures with helical appearance [34]. Interaction between Klebanoff streaks and the instability waves seems to drive the helical instability as the breakdown is activated at relatively low streak amplitude (Fig. 26). This inner instability grows in the high-shear region between low- and high-speed streaks.

The instability waves are still apparent when the intensity is increased even higher, to $Tu \sim 2\%$ (case 3). Exponential amplification is dominant in the spectra for v' but the u' spectra are dominated by Klebanoff streaks. The local u'_{rms} profiles have peak magnitude an order of magnitude higher than v'_{rms} and w'_{rms} . For case 3, breakdown is mostly via inner modes. A few instances of outer modes were also seen. The Klebanoff streaks at high Tu play a dual role: Stronger streaks are more unstable and prone to outer instability; also, they distort the mean boundary-layer profile, which stabilizes its primary eigenmodes. The present simulations indicate that instability waves contribute substantially to transition in APG and that their amplitude can be comparable to Klebanoff streaks [16]. Under the conditions of the present numerical experiments, transition in APG boundary layers beneath free-stream turbulence is therefore truly mixed-mode transition.

ACKNOWLEDGMENTS

This work was supported by NSF Grant No. CBET-1228195. Computer time was provided by the Extreme Science and Engineering Discovery Environment (XSEDE).

-
- [1] R. G. Jacobs and P. A. Durbin, Shear sheltering and the continuous spectrum of the Orr-Sommerfeld equation, *Phys. Fluids* **10**, 2006 (1998).
 - [2] T. A. Zaki and S. Saha, On shear sheltering and the structure of vortical modes in single- and two-fluid boundary layers, *J. Fluid Mech.* **626**, 111 (2009).
 - [3] M. T. Landahl, A note on an algebraic instability of inviscid parallel shear flows, *J. Fluid Mech.* **98**, 243 (1980).
 - [4] O. M. Phillips, Shear-flow turbulence, *Annu. Rev. Fluid Mech.* **1**, 245 (1969).
 - [5] P. A. Durbin, Perspectives on the phenomenology and modeling of boundary layer transition, *Flow, Turbul. Combust.* **99**, 1 (2017).
 - [6] T. A. Zaki, From streaks to spots and on to turbulence: Exploring the dynamics of boundary layer transition, *Flow, Turbul. Combust.* **91**, 451 (2013).
 - [7] A. V. Boiko, K. J. A. Westin, B. G. B. Klingmann, V. V. Kozlov, and P. H. Alfredsson, Experiments in a boundary layer subjected to freestream turbulence. Part II. The role of TS waves in the transition process, *J. Fluid Mech.* **281**, 219 (1994).
 - [8] C. Cossu and L. Brandt, On Tollmien-Schlichting like waves in streaky boundary layers, *Eur. J. Mech. B* **23**, 815 (2004).

- [9] Y. Liu, T. A. Zaki, and P. A. Durbin, Boundary-layer transition by interaction of discrete and continuous modes, *J. Fluid Mech.* **604**, 199 (2008).
- [10] R. Bose and P. Durbin, Transition to turbulence by interaction of free-stream and discrete mode perturbations, *Phys. Fluids* **28**, 114105 (2016).
- [11] G. J. Walker and J. P. Gostelow, Effects of adverse pressure gradients on the nature and length of boundary layer transition, *J. Turbomach.* **112**, 196 (1989).
- [12] J. P. Gostelow, A. R. Blunden, and G. J. Walker, Effects of free-stream turbulence and adverse pressure gradients on boundary layer transition, *J. Turbomach.* **116**, 392 (1994).
- [13] J. D. Hughes and G. J. Walker, Natural transition phenomena on an axial flow compressor blade, *J. Turbomach.* **123**, 392 (2001).
- [14] T. Zaki, J. Wissink, W. Rodi, and P. Durbin, Direct numerical simulations of transition in a compressor cascade: The influence of free-stream turbulence, *J. Fluid Mech.* **665**, 57 (2010).
- [15] S. Nagarajan, S. K. Lele, and J. H. Ferziger, Leading-edge effects in bypass transition, *J. Fluid Mech.* **572**, 471 (2007).
- [16] P. Corbett and A. Bottaro, Optimal perturbations for boundary layers subject to stream-wise pressure gradient, *Phys. Fluids* **12**, 120 (2000).
- [17] Y. S. Kachanov, Physical mechanisms of laminar-boundary-layer transition, *Annu. Rev. Fluid Mech.* **26**, 411 (1994).
- [18] L. Kleiser and T. A. Zang, Numerical simulation of transition in wall-bounded shear flows, *Annu. Rev. Fluid Mech.* **23**, 495 (1991).
- [19] P. Andersson, L. Brandt, A. Bottaro, and D. S. Henningson, On the breakdown of boundary layers streaks, *J. Fluid Mech.* **428**, 29 (2001).
- [20] N. J. Vaughan and T. A. Zaki, Stability of zero-pressure-gradient boundary layer distorted by unsteady Klebanoff streaks, *J. Fluid Mech.* **681**, 116 (2011).
- [21] M. J. P. Hack and T. A. Zaki, Streak instabilities in boundary layers beneath free-stream turbulence, *J. Fluid Mech.* **741**, 280 (2014).
- [22] X. Wu and P. A. Durbin, Evidence of longitudinal vortices evolved from distorted wakes in a turbine passage, *J. Fluid Mech.* **446**, 199 (2001).
- [23] K. P. Nolan and T. A. Zaki, Conditional sampling of transitional boundary layers in pressure gradients, *J. Fluid Mech.* **728**, 306 (2013).
- [24] R. Bose, Mixed mode transition to turbulence in boundary layers, Ph.D. thesis, Iowa State University, Ames, Iowa, 2016, <https://lib.dr.iastate.edu/etd/15882>.
- [25] F. M. White, *Viscous Fluid Flow*, 2nd ed. (McGraw-Hill, New York, 1991).
- [26] L. Brandt, P. Schlatter, and D. S. Henningson, Transition in boundary layers subject to free-stream turbulence, *J. Fluid Mech.* **517**, 167 (2004).
- [27] R. G. Jacobs and P. A. Durbin, Simulations of bypass transition, *J. Fluid Mech.* **428**, 185 (2001).
- [28] A. D. D. Craik, Nonlinear resonant instability in boundary layers, *J. Fluid Mech.* **50**, 393 (1971).
- [29] V. I. Borodulin, Y. S. Kachanov, and A. P. Roschektayev, Turbulence production in an APG-boundary-layer transition induced by randomized perturbations, *J. Turbulence* **7**, N8 (2006).
- [30] V. I. Borodulin, Y. S. Kachanov, and A. P. Roschektayev, Experimental detection of deterministic turbulence, *J. Turbulence* **12**, N23 (2011).
- [31] T. Herbert, Secondary instability of boundary layers, *Annu. Rev. Fluid Mech.* **20**, 487 (1988).
- [32] Y. Liu, T. A. Zaki, and P. A. Durbin, Floquet analysis of secondary instability of boundary layers distorted by Klebanoff streaks and Tollmien-Schlichting waves, *Phys. Fluids* **20**, 124102 (2008).
- [33] J. R. Brinkerhoff and M. I. Yaras, Numerical investigation of transition in a boundary layer subjected to favourable and adverse streamwise pressure gradients and elevated free stream turbulence, *J. Fluid Mech.* **781**, 52 (2015).
- [34] R. Bose and P. Durbin, Helical modes in boundary layer transition, *Phys. Rev. Fluids* **1**, 073602 (2016).
- [35] C. Cossu and L. Brandt, Stabilization of Tollmien-Schlichting waves by finite amplitude optimal streaks in the Blasius boundary layer, *Phys. Fluids* **14**, L57 (2002).